# Supplementary Material for: Novel electron scattering experiment finds small proton radius.

## Advantages of the Magnetic-spectrometer-free Method

A precision extraction of $r_p$ requires the $e-p$ elastic cross section to be measured with sub-one percent accuracy over a wide range of $Q^2$, extending down to very low values of $Q^2$. Previous $e-p$ measurements used for radius extractions have been performed with magnetic spectrometers that have very limited angular acceptance [1,2]. The small acceptance limits the $Q^2$ range covered in a single setting to a very small fraction of the desired range, requiring the magnetic spectrometers to be physically moved to many different angles. Each move of the spectrometer results in a new set of systematic offsets for critical parameters such as the angle of the spectrometer with respect to the incoming beam, effective target length, geometric and momentum acceptance, etc. As a result, the radius extraction from magnetic spectrometer data requires one normalization parameter for each angle setting, giving rise to a vast multitude of parameters which could negatively impact the precision of the radius extraction. In the PRad experiment the full $Q^2$ range covered at each beam energy was collected in a single fixed location of the calorimeter and gas electron multiplier (GEM) detector. All readout elements were frozen in location for the entire experiment, thus, eliminating the multitude of normalization parameters. Only two normalization parameters were used in the PRad $r_p$ extraction, corresponding to the two beam energies used during the experiment. Moreover, the calculation of the scattering cross section for a particular $Q^2$ bin requires precise

knowledge of the solid angle within which the scattered particles are detected. In a magnetic spectrometer the scattered particles travel through a magnetic field, which bends and distorts the particle trajectories en route to the detectors. Thus the determination of the solid angle at the reaction vertex requires complex unfolding of the influence of the magnetic field. In the PRad experiment the scattered electrons have straight line-of-sight paths from target to the detectors. The transverse $X - Y$ position of these paths are determined with high accuracy using the GEM detectors. This position information combined with the constraints on the opening angle of the Møller electron pair detected in the experiment, allows the solid angle to be determined with high-precision for each $Q^2$ bin. These advantages of the magnetic-spectrometer-free method allow for a high-precision extraction of $r_p$.

## The HyCal Calorimeter and the GEM Detector

The PrimEx HyCal calorimeter [3] is a hybrid electromagnetic calorimeter consisting of two different types of shower detectors, 576 Pb-glass modules ($3.82 \times 3.82 \times 45$ cm$^3$) and 1152 $PbWO_4$ crystal modules ($2.05 \times 2.05 \times 18.0$ cm$^3$). The calorimeter with its $116 \times 116$ cm$^2$ cross sectional area was located in the beam line at a distance of 5.5 m from the hydrogen target. The $PbWO_4$ crystals were wrapped in 100 $\mu$m VM2000 reflective material to improve light collection and then in 36 $\mu$m of Tedlar for light isolation. The crystals were attached to Hamamatsu R4125HA photo-multiplier tubes with optical grease. The Pb-glass modules were wrapped in 25 $\mu$m aluminized mylar foil and the light was detected in Russian- made FEU 84-3 photo-multiplier tubes. The electron beam passed through a $4.0 \times 4.0$ cm$^2$ hole in the central part of HyCal ($2 \times 2$ $PbWO_4$ modules are

removed from the assembly).

The gain stability of each channel is monitored using a blue LED based light monitoring system (LMS) where the pulsed LED light was distributed to each detector module via optical fibers attached to the front face of each module. In addition, the light produced by the LED source was delivered to three reference PMTs, which had thin scintillators and $^{241}$Am radioactive sources attached. The light from the LED was periodically (once every $\sim$ hour long run) injected into each HyCal module. Typically less than 5% gain fluctuations were observed during the entire experiment. The LMS signal was used to correct the calibration constants and thus the position of the elastic peak in each module. After this correction, the fluctuation of the elastic peak position was $<$0.5%, which is much smaller than the energy resolution of HyCal. Figure S1 shows the stability of the gain as monitored by the LMS over the period of the experiment.

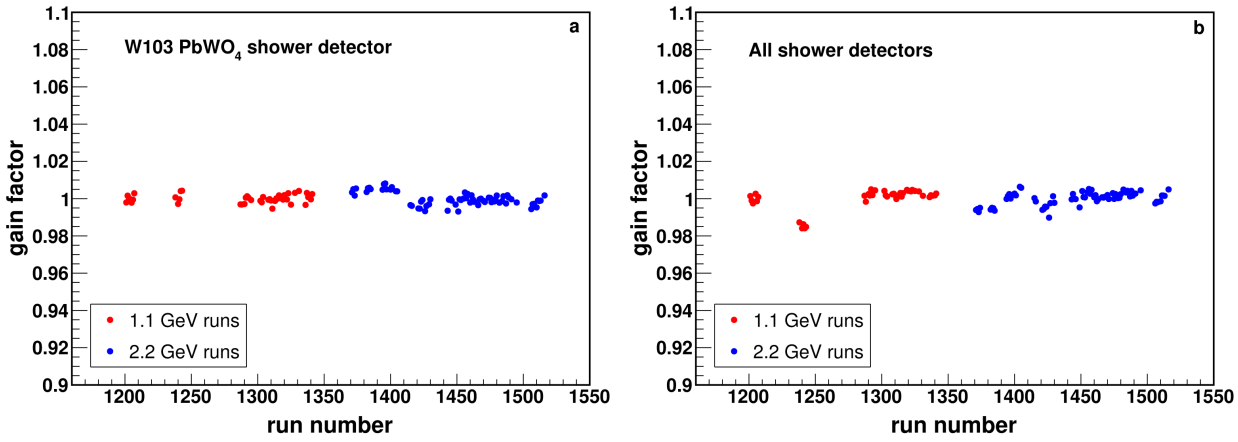


Figure S1: **(a)** The gain as monitored by the LMS for one $PbWO_4$ module as function of run-number (time) and **(b)** the gain averaged over all HyCal modules for the entire experiment.

A Gas Electron Multiplier (GEM) detector layer was located just in front of the calorimeter. The GEM layer was built to match the area of the calorimeter and was made of two large area GEM detectors, each with an active area of 123 cm $\times$ 55 cm, arranged so that there is a narrow overlap area in the middle. A hole with a 4 cm diameter was built into the GEM detectors at the center of the active area allowing for the passage of the beamline. The GEM detectors were triple GEM foil structures followed by a 2D x-y strip readout layers. Each pair of GEM foils had $2\times4$ grid of thin dielectric spacers between them to prevent them from coming into contact with each other. Each large area GEM foil was sub-divided into 60 sectors; the 61.5 cm long and 1.83 cm wide sectors were separated by narrow (100 $\mu$m) margins. The GEM efficiency loss due to the presence of the spacers and sector margins was measured using data and was modeled in the simulation.

The possible contamination due to photon induced GEM hits was studied using the simulation. Such contamination is highly suppressed because of the angle dependent energy cuts used to select $e-p$ and $e-e$ events and the matching condition between the GEM and the HyCal (the GEM hits projected to the HyCal assuming they are coming from the target, must agree with the HyCal hits within 6 $\sigma$ of the detector resolution). If the photons satisfy $e-p$ or $e-e$ energy cuts for HyCal, they have about 1.5% - 2% chance to produce matching GEM hits and contaminate the data. This number is dominated by contributions from the vacuum window, but also contains contributions from other sources, such as the GEM frames and the GEM foils. The number of photons relative to the electrons was estimated by varying the energy cut for the elastic peak ($1\sigma-4\sigma$, where $\sigma$ is the detector resolution) and noting the change in the GEM efficiency. The photon to electron ratio was estimated to be at the most 0.4% - 0.5% for most of the energy cuts. This ex-

perimental value of the photon to electron ratio agrees well with the simulated value for the same energy cuts. The contamination is the product of the photon to electron ratio and the chance that the photon can produce a matching pair of hits in the GEM and HyCal. Thus the upper bound of contamination due to photon induced GEM hits is 0.01%.

## The Windowless Target

A novel addition in this experiment is the usage of a windowless hydrogen gas flow target having a density of $\sim 2 \times 10^{18}$ hydrogen atoms/cm$^2$. This is a relatively high density for the typical windowless gas flow targets, used before mainly as internal targets. This high density was reached by flowing cryo-cooled hydrogen gas (at 19.5° K) through the target cell made of a 40 mm long and 63 mm diameter cylindrical shaped pipe within a copper block. The side windows of this cell was covered by a thin (7.5 $\mu$m) kapton film with 2 mm holes at the center for the passage of the electron beam through the target. Two high capacity (3400 l/s) turbo-molecular pumps were used to keep a pressure of $\sim 2.3$ mtorr in the chamber (outside the cell), while the pressure inside the cell was maintained at $\sim 470$ mtorr. Two additional high capacity turbo-molecular pumps, placed immediately upstream and downstream of the target chamber, were used to maintain the beamline vacuum at a pressure of $2 \times 10^{-5}$ torr. During the experiment a number of pressure gauges and temperature sensors were used to monitor the gas pressure and temperatures at multiple locations across the entire target system. These measured temperature values, together with the inlet gas flow rate, pumping speeds of the pumps, and the detailed geometry of the target system were used to simulate the hydrogen density profile in the target using the COMSOL Multiphysics ® simulation

package. The average pressure obtained from the simulation agreed with the measured values within 2 mTorr for both the target cell and the target chamber, under the PRad production running conditions.

## Background Subtraction

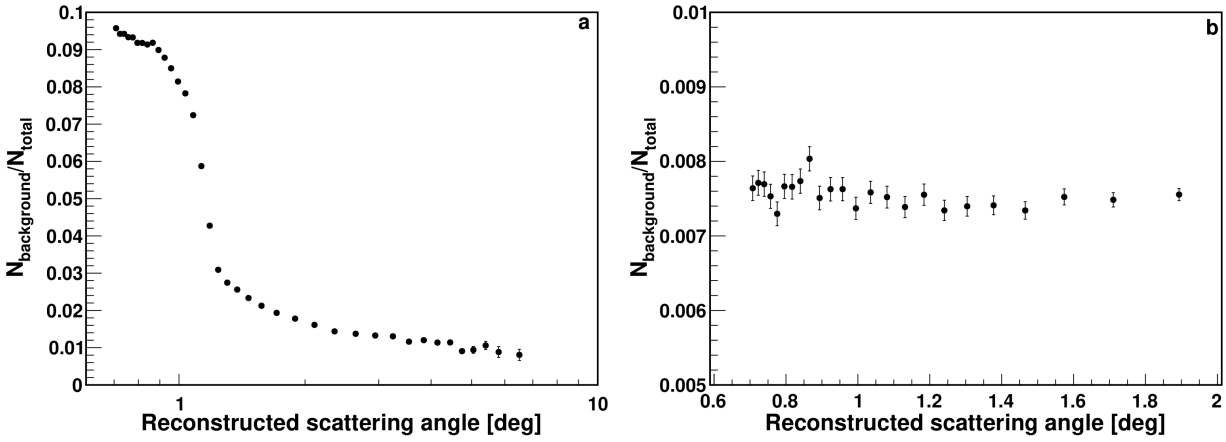


Figure S2: **(a)** Relative background yield for $e-p$ and **(b)** $e-e$ events for the 2.2 GeV electron beam energy, determined from beam incident on an empty target.

The PRad experiment was conducted with 1.1 GeV and 2.2 GeV electron beams from the CEBAF accelerator incident on cryo-cooled hydrogen atoms flowing through a windowless target cell. The scattered electrons after traversing the vacuum chamber were detected in the GEM and the HyCal electromagnetic calorimeter [3]. They included electrons from $e-p$ and Møller scattering processes. The energy of the detected electron(s) for each event was measured by HyCal. The transverse ($X-Y$) positions was measured by the GEM detector and used to calculate the $Q^2$ for that event. The window-less target used in the PRad experiment eliminated all background from direct impact of the electron beam on the target cell's front and back windows. Consequently, the

primary background was due to the interaction of the beam halo with the materials surrounding the beam line, such as the upstream beam halo blocker (the dominant source) and the target cell walls. The beam interacting with the residual hydrogen gas in the beam-line was another source of background. These backgrounds account for $\sim$10% of the 2.2 GeV $e-p$ elastic events at very forward angles ($< 1.1^{\circ}$) but quickly reduce to below 2% elsewhere, as shown in Figure S2 (a). On the other hand, the beam-line background contribution to the $e-e$ yield is highly suppressed because the pair of $e-e$ electrons are detected in coincidence. It accounts for $\sim$0.8% of the 2.2 GeV $e-e$ events, as shown in Figure S2 (b). For the 1.1 GeV data, the background contribution is higher due to the relatively worse beam conditions. It accounts for $\sim$30% of the $e-p$ elastic events at angles $< 1.1^{\circ}$ and reduces to less than 10% elsewhere, and $\sim$2.1% of $e-e$ events at 1.1 GeV are due to beam-line background.

The experimental background was measured every few hours with the electron beam incident on an empty target cell. During these runs 2.9 mTorr of $H_2$ gas was allowed into the target chamber to mimic the residual gas present during the production runs. Data with the electron beam incident on an evacuated chamber and cell were also collected a few times over the course of the experiment. The charge normalized $e-p$ elastic and $e-e$ yields from the empty target cell were subtracted from the yield of the $H_2$ filled target cell, effectively removing the background contribution. The time variation of the background subtraction was studied by performing the background subtraction using different combinations of the empty target runs, such as, the empty target run before or after the corresponding production run, or the average of these two runs. The time variation was used as a systematic uncertainty due to the background subtraction. This uncertainty is negligible for the

2.2 GeV data, but is one of the significant uncertainties for the 1.1 GeV data (see Table S1).

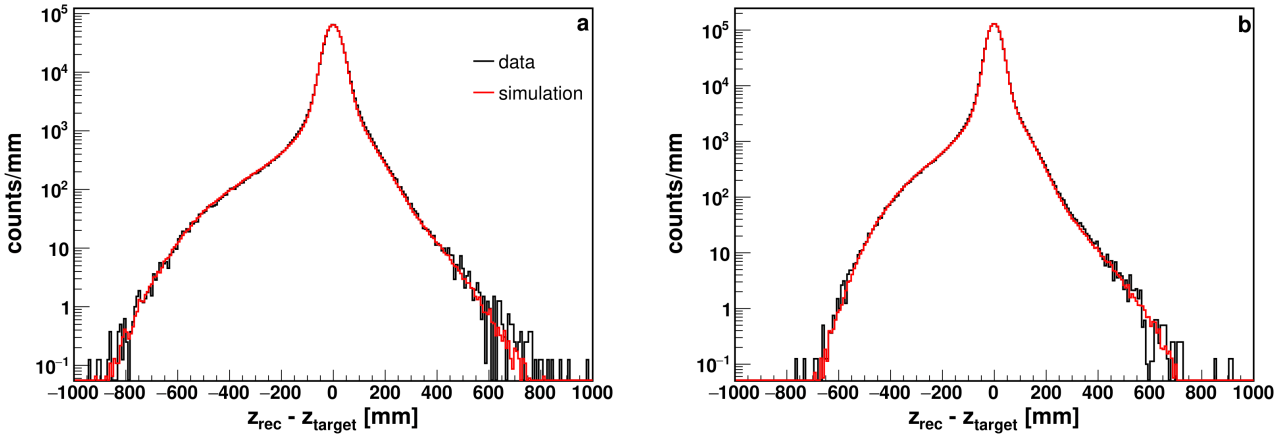


Figure S3: **(a)** The difference between the reconstructed vertex position along the beam ($z_{\rm rec}$) and the center of the target along the beam direction ($z_{\rm target}$) for $e-e$ events at 1.1 GeV beam energy. **(b)** The same quantity at 2.2 GeV beam energy.

Further, to demonstrate that the background subtraction procedure is reliable, the reconstructed vertex position along the beam (vertex-$z$) for the $e-e$ events was studied. The vertex-$z$ is reconstructed using Eq. 1. The excellent agreement between the data and the simulated vertex-$z$ positions shown in Figure S3 indicate that the target gas density profile is as expected and well modeled in the simulation and the background subtraction procedure is robust. The majority of contribution to the tails of the vertex-$z$ distribution is from radiated $e-e$ events and not from residual gas outside the target cell. To estimate the systematic uncertainty due to any residual gas outside the target cell, more than 10 different gas density profiles were studied. These profiles ranged from no-gas outside the cell to a profile that produced $>30\%$ more events at +/- 300 mm away from target center compared to the default density profile used in the simulation. The variations in cross section and $r_p$ for these density profiles were used as part of the uncertainty due to

beam-line background.

## Calibration and Event Reconstruction

The reconstruction of the energy deposited in HyCal relied on a careful calibration of the calorimeter. The calorimeter was calibrated using a tagged photon beam produced by a 1.1 GeV electron beam incident on the thin wire target of the Hall-B tagger [4]. Each $PbWO_4$ and Pb-glass module of the calorimeter was exposed to the tagged photon beam, one at a time, by sequentially transporting the entire calorimeter in a snake-like pattern. The energy deposited in the calorimeter is reconstructed using a clustering algorithm [3], which assigns a constant parameter to each module such that the reconstructed energy agreed with the incident photon energy as determined by the Hall-B tagger. In addition, energy deposited by $e - p$ and $e - e$ events collected during the experiment were used to fine tune the constant parameters, such that the centroid of the reconstructed elastic peak agreed with its expected value to better than $0.1\%$.

The total energy deposited in HyCal determined the trigger for the accepted events. The trigger efficiency was evaluated during the calibration of the calorimeter with the tagged photon beam. During the calibration, the trigger was provided by the tagger and the HyCal trigger efficiency was given by the ratio of the HyCal events to the tagger events. Trigger efficiencies for both $PbWO_4$ and Pb-glass portion of HyCal typically reached a plateau at about 99.9% when the total energy deposited exceeded 400 MeV ( Figure S4). A few low efficiency modules were identified and discarded during the data analysis.

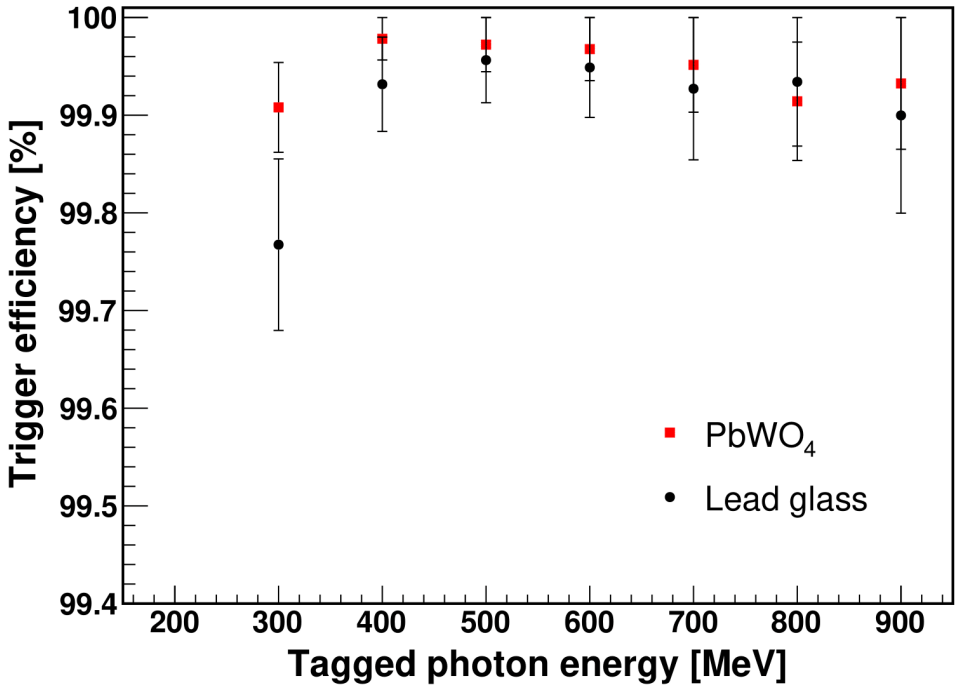


Figure S4: Typical trigger efficiency for the $PbWO_4$ and Pb-glass portion of HyCal.

The determination of $Q^2$ for each event relies on the accurate reconstruction of the scattered electron angle, which in turn relies on the precise knowledge of the longitudinal ($z$) distance from the center of the target to the detectors, and the transverse position of the beam. Both of these were determined in the PRad experiment using $e-e$ events where the two scattered electrons were detected in coincidence. Momentum conservation constrains the two $e-e$ electrons to be in the same plane relative to the reaction vertex (co-planarity), therefore, the lines connecting the detector hit position of the two electrons to the target must intersect at the transverse location of the beam. This technique was applied for each data run to precisely determine the beam's transverse position to within 50$\mu$m. The $z$ distance between the target center and the detectors was evaluated after the center of the beam had been determined. Using energy and momentum conservation and the

kinematics of $e - e$ scattering, one obtains the relation,

$$z = \sqrt{\frac{(m_e + E_b)R_1R_2}{2m_e}}, \tag{1}$$

where $m_e$ is the mass of an electron, $E_b$ is the beam energy and $R_1$ and $R_2$ are the distance of the detector hit positions relative to the center of the beam. The $z$ distance determined from the data collected with 1.1 GeV and 2.2 GeV electron beam energy agreed with each other to within 1 mm ($\sim 0.02\%$) and they also agreed with the surveyed positions to the same level.

The comprehensive Monte Carlo simulation of the PRad experimental setup played an essential role in the reconstruction of the energy deposited in HyCal. Simulated charged particles with known energy and angles that produce a signal in the calorimeter were utilized to generate a collection of profiles of the signal as distributed among the calorimeter modules (cluster profiles). The simulated cluster profiles are compared with the cluster profiles for each detected event, where all the calorimeter modules with signal in a neighbouring module were grouped together (also know as "island clustering"). Further, the clusters from detected events are iteratively subdivided until a best match is achieved with the simulated cluster profiles. The energy and position of each cluster is then determined from the centre of gravity of the cluster with logarithmic weighting corresponding to the exponential decay of the signal strength with distance from the hit centre. Corrections arising from the non-linear response of the calorimeter modules, signal leakage at the gaps between the modules or at the detector boundaries were obtained from the calibration data and applied to the reconstructed energy and position. Finally, the reconstructed position of the event was substituted with the reconstructed position of the best matching GEM hit within a coincidence time window of $\sim$200 ns. The variation of the reconstructed energy and position and their

corrections as a function of the parameters of the clustering and matching procedures was studied in the simulation, and was incorporated into the systematic uncertainty.

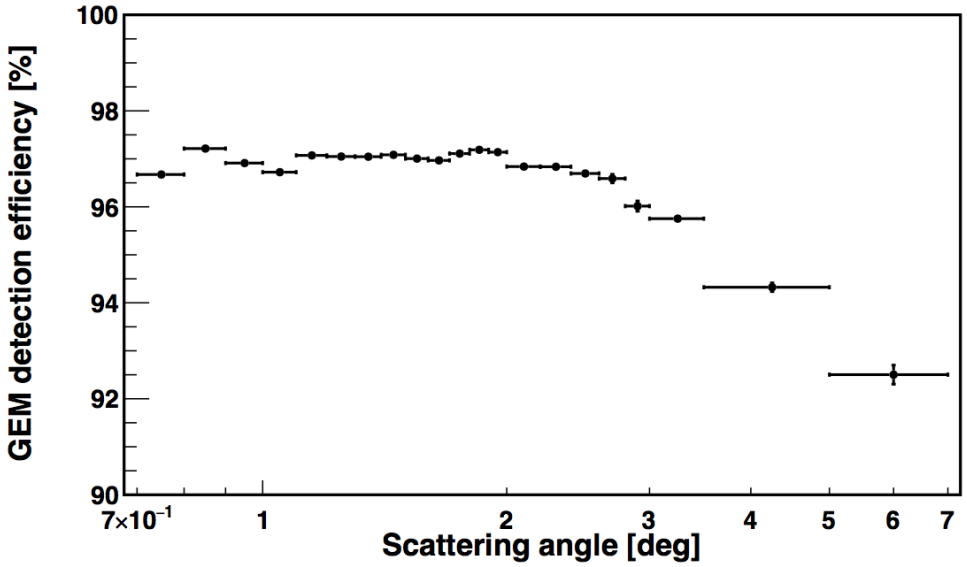


Figure S5: The GEM detector efficiency as a function of the scattering angle. The statistical uncertainty of each point is included but is smaller than the marker size.

The matching of the HyCal and GEM hits relied on a careful determination of the efficiency of the GEM detector. The efficiency of the GEM detector was determined using three different methods. During the calibration of the calorimeter with a tagged photon beam, two scintillators were placed in the path of the photon beam to convert a fraction of the photons into electron-positron pairs. These charged particles were then used to determine the efficiency of the GEM detectors. The other two methods used the $e - p$ elastic and $e - e$ events, respectively, from the production runs to determine the efficiency. The efficiencies obtained from all three methods agree with each other to better than $1\%$. A plot of the GEM efficiency determined from the $e - p$

elastic scattering events is shown in Figure S5. The consistency in the GEM efficiency corrected super-ratio of the experimental to the simulated $(e-p)/(e-e)$ ratio between the four quadrants, as shown in Figure S8, and the consistency between the three methods used to determine the GEM efficiency, demonstrates that the GEM efficiency is accurate. The GEM efficiency was also shown to be independent of the elastic cut used for event selection, this further confirms the robustness of the GEM efficiency determination.

## Angular Resolution and $Q^2$ Resolution

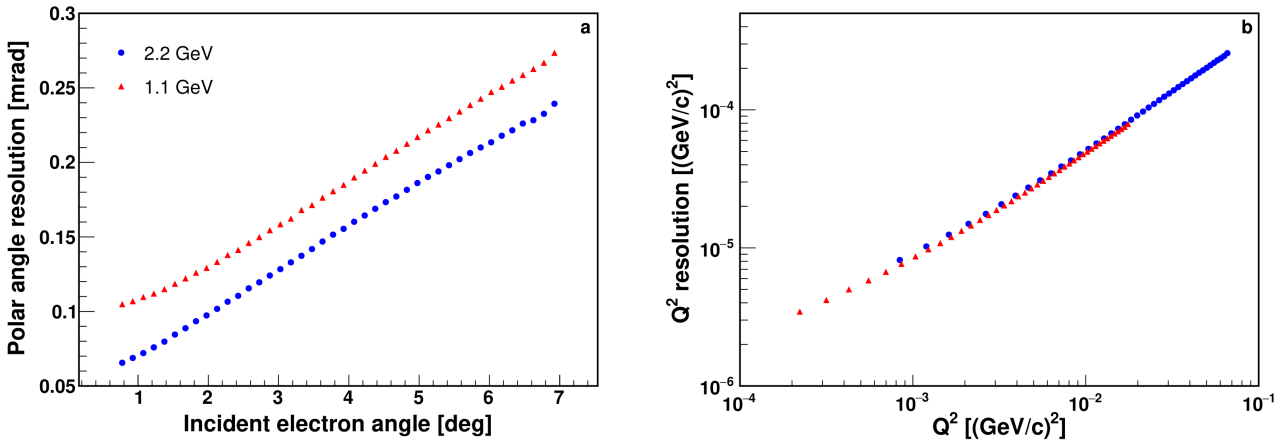


Figure S6: **(a)** The angular resolution as a function of scattering angle achieved in the experiment at 1.1 GeV (red) and 2.2 GeV (blue) electron beam energy. **(b)** The $Q^2$ resolution as a function of $Q^2$.

The energy of the electron beam delivered by the Continuous Electron Beam Accelerator Facility (CEBAF) accelerator was measured with an uncertainty of 0.5 MeV at 1.1 GeV and 1.5 MeV at 2.2 GeV, and it had an energy spread of $3 \times 10^{-5}$. The pair of GEM detectors that were used as coordinate detectors helped achieve an angular resolution of 0.06/0.1 mrad for the smallest

angle for the 2.2/1.1 GeV beam energy and 0.24/0.27 mrad for the largest angle covered at 2.2/1.1 GeV beam energy. The angular resolution for $e-p$ scattering as a function of the scattering angle is shown in Figure S6 (a) for the two beam energies. The energy and angular resolutions were used to obtain the $Q^2$ resolution shown in Figure S6 (b). The angular resolution was used to determine the size of the $Q^2$ bins used to extract the cross section and electric form factor from the experimental yield.

## Monte Carlo Simulation

The comprehensive Monte Carlo simulation played a critical role in the extraction of the next-to-leading order $e-p$ elastic cross section from the experimental yield. The simulation consists of two separate event generators built for the $e-p$ and $e-e$ processes, and they include next-to-leading order contributions to the cross section (radiative corrections), such as Bremsstrahlung, vacuum polarization, self-energy and vertex corrections. The calculations of the $e-p$ elastic and Møller radiative corrections are performed within a covariant formalism, without the usual ultra relativistic approximation [5], where the mass of the electron is neglected. The two generators also include contributions from two-photon exchange processes [6–8]. A second independent $e-p$ elastic event generator [9] was used as a cross check. The radiative corrections to the proton, which are typically neglected, were included in this generator. The two $e-p$ generators were found to be in excellent agreement.

Inelastic $e-p$ scattering events were included in the simulation using an empirical fit [10]

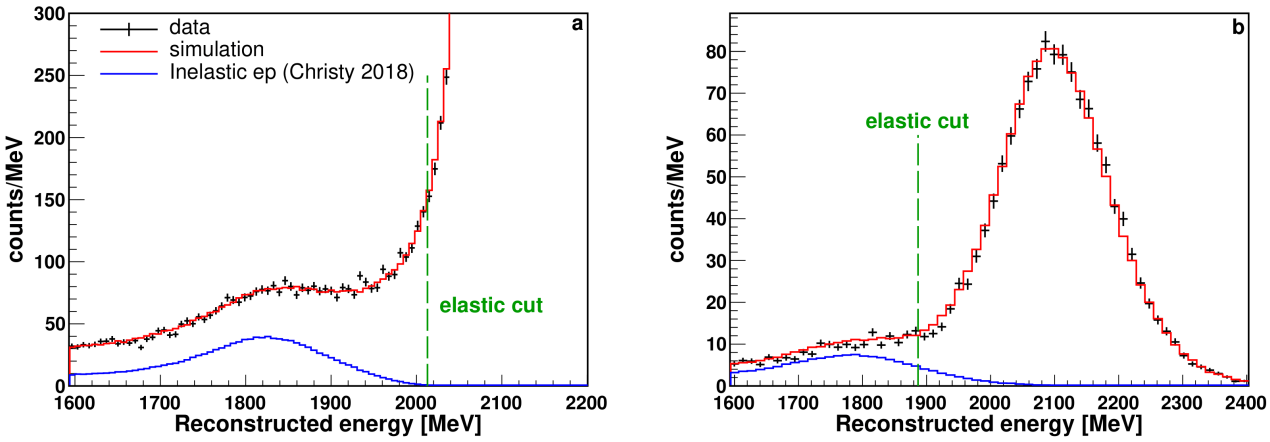


Figure S7: Comparison between reconstructed energy spectrum from the 2.2 GeV data (black) and simulation (red) for: **(a)** the $PbWO_4$ modules which cover scattering angles from 3.0° to 3.3°, corresponding to $Q^2$ around 0.014 (GeV/c)$^2$; **(b)** the Pb-glass modules which cover scattering angles from 6.0° to 7.0°, corresponding to $Q^2$ around 0.059 (GeV/c)$^2$ (largest $Q^2$ for PRad). Blue histograms show the inelastic $e-p$ contribution from the simulation. The green dash lines indicate the minimum elastic cut for selecting $e-p$ event for the two different detector modules. Due to the large difference in amplitudes, the elastic $e-p$ peak (amplitude 2800 counts/MeV) is not shown in **(a)**, to display the $\Delta$-resonance peak.

to the $e-p$ inelastic scattering world data. Inelastic $e-p$ scattering contributes a background to the $e-p$ elastic spectrum which, when included in the simulation was able to reproduce the measured elastic $e-p$ spectrum as shown in Figure S7. In the $PbWO_4$ segment of the calorimeter, there was a clear separation between the elastic and inelastic $e-p$ events, and it was established that the position and amplitude of the $\Delta$-resonance peak in the simulation agreed with the data to better than 0.5% and 10%, respectively. The $\Delta$-resonance contribution was found to be negligible ($\ll 0.1\%$) for the $PbWO_4$ segment of the HyCal, and no more than 0.2% and 2% for the Pb-glass segment, at 1.1 GeV and 2.2 GeV, respectively. The generated scattering events were propagated within the Geant4 simulation package, which included the detector geometry and materials of the PRad setup. This enabled a proper accounting of the external Bremsstrahlung of particles passing through various materials along its path. The simulation included photon propagation and digitization of the simulated events. These steps were critical for the precise reconstruction of the position and energy of each event in the HyCal.

**Cross Section and Electric Form Factor**

The $e-p$ elastic cross section extracted from the PRad data is normalized relative to the Møller scattering cross section. At forward angles ($< 3.0^\circ$ at 1.1 GeV and $< 1.6^\circ$ at 2.2 GeV), where the smaller Møller angular acceptance overlaps with the $e-p$ angular acceptance, the $e-p$ elastic yield was normalized to the Møller yield in each angular bin of the data. This enables a cancellation of the energy-independent contributions of the detector acceptance and efficiency, for example the GEM detector efficiency. In addition, over the full angular range of the experiment, the $e-p$

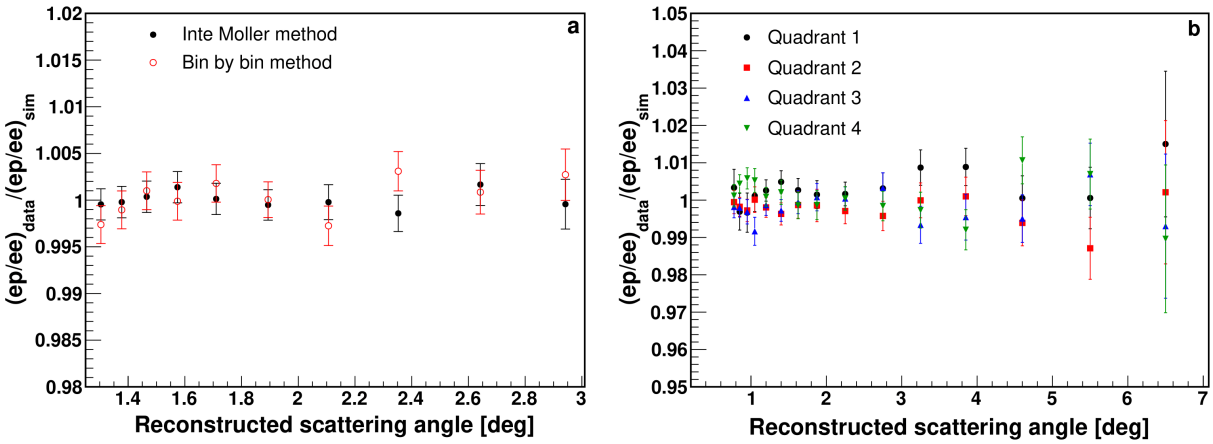


Figure S8: **(a)** 1.1 GeV super-ratio of the experimental $(e-p)/(e-e)$ yield and the simulated $(e-p)/(e-e)$ yield, obtained using the bin by bin method (open red circles) and the integrated Møller method (solid black dots). **(b)** The super-ratio calculated separately for each quadrant of the HyCal detector.

elastic yield for each angular bin was normalized to the integrated Møller yield over a selected angular range ($1.3^\circ - 3.0^\circ$ at 1.1 GeV and $1.3^\circ - 2.0^\circ$ at 2.2 GeV). The cross sections obtained using both methods were found to be consistent with each other, as shown in Figure S8 (a). The results obtained using these two methods differ by $< 0.2\%$ on the average, which is consistent with the typical uncertainty of the GEM efficiency correction obtained from simulation studies. To minimize the systematic uncertainties in extracting the final cross sections the bin-by-bin method was utilized for the forward angles and the integrated Møller method was applied everywhere else.

The azimuthal symmetry of the extracted cross section was verified by comparing the super-ratio of the data $(e-p)/(e-e)$ and the simulated $(e-p)/(e-e)$ yields, separately from each

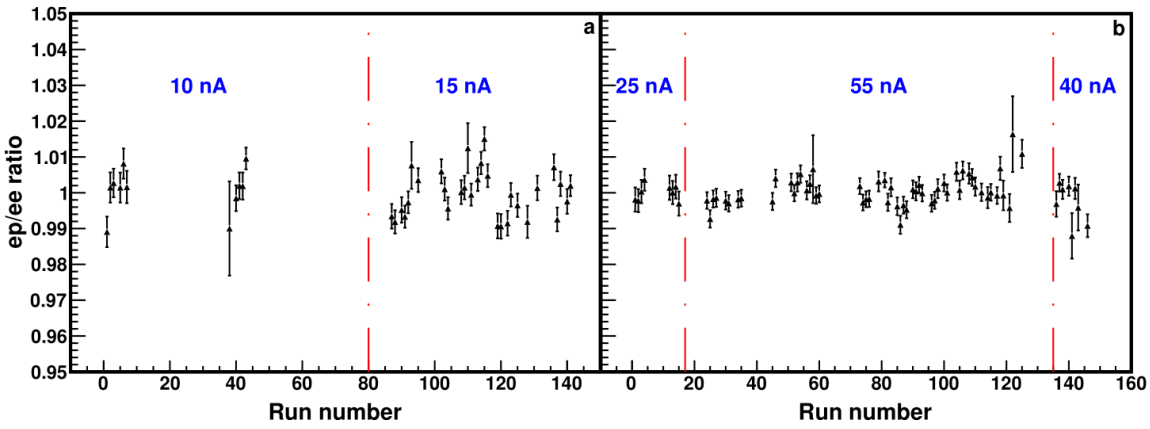


Figure S9: **(a)** Experimental $(e-p)$/$(e-e)$ ratio as a function of run number (time), for the 1.1 GeV electron beam energy and **(b)** for the 2.2 GeV beam energy. Runs taken with different beam currents are separated by red dash lines and marked by the blue labels.

quadrant of the HyCal calorimeter. The super-ratio from each quadrant was found to be consistent with each other within the statistical uncertainty, as shown in Figure S8 (b). The invariance of the experimental $(e-p)$/$(e-e)$ ratio over time was also verified as shown in Figure S9. Moreover, the weighted average for runs taken with different beam currents are statistically consistent with each other. In addition, the consistency between the $PbWO_4$ and Pb-glass modules of the HyCal was verified by comparing the super-ratio with and without using the Pb-glass modules. The super-ratio in the angular range where the $PbWO_4$ and Pb-glass modules overlapped was also studied. As shown in Figure S10, the super-ratio is consistent with each other for the different combination of detector modules. Finally, the extracted cross section for the 1.1 GeV and 2.2 GeV electron beam energies are shown in Figure S11.

The $e-p$ elastic differential cross sections in the one-photon exchange limit can be written in

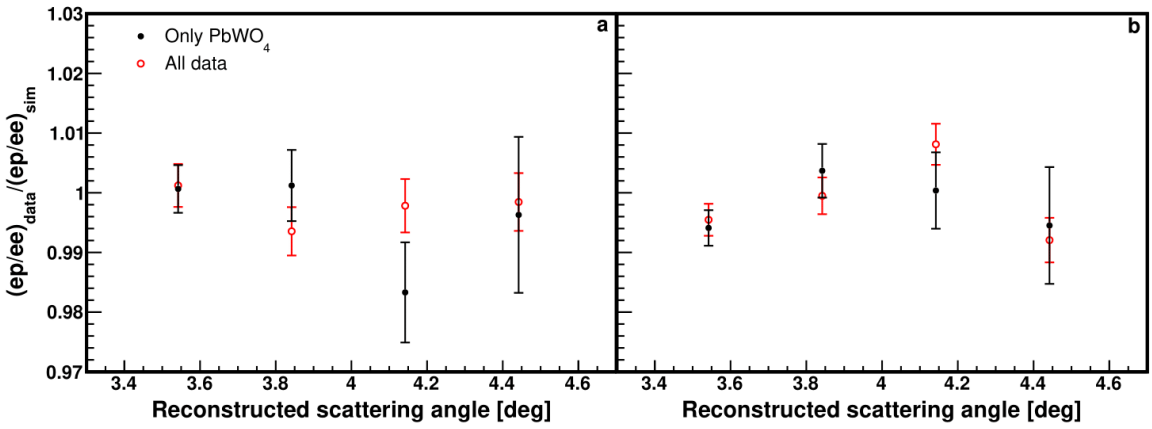


Figure S10: The super-ratio when using only $PbWO_4$ modules and when using all modules for the angular region where both $PbWO_4$ and Pb-glass modules have overlapping coverage, shown for the **(a)** 1.1 GeV and **(b)** 2.2 GeV electron beam energy.

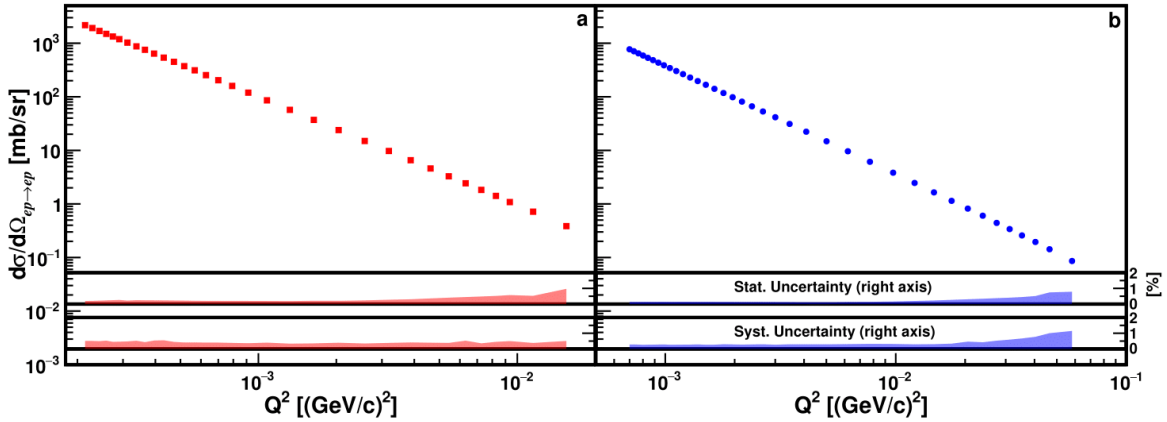


Figure S11: **(a)** Differential cross sections for the $e-p$ elastic process from the 1.1 GeV data, and **(b)** the 2.2 GeV data set. Statistical and systematic uncertainties are shown as separate bands and are scaled to the right axes of each plot.

terms of the so called Rosenbluth formula [11] which relates it to the proton electric form factor ($G_E^p$) and magnetic form factor ($G_M^p$). In the very low $Q^2$ region covered by the PRad experiment, the

$e-p$ elastic scattering cross section is dominated by the contribution from $G_E^p$ and it was extracted from the measured $e-p$ elastic cross section by assuming the Kelly parametrization for $G_M^p$ [12]. The uncertainty in the extracted $G_E^p$ introduced by the choice of the $G_M^p$ parametrization was studied by using a wide variety of parametrizations for $G_M^p$ [2,13–16], including the standard dipole form. The relative difference between the extracted $G_E^p$ for each of these parametrizations with respect to the Kelly parametrization [12] is shown in Figure S12. The extracted $G_E^p$ varies by $\sim 0.2\%$ at $Q^2 = 0.06$ $(\mathrm{GeV/c})^2$, the largest $Q^2$ accessed by the PRad experiment, and $< 0.01\%$ in the $Q^2 < 0.01$ $(\mathrm{GeV/c})^2$ region.

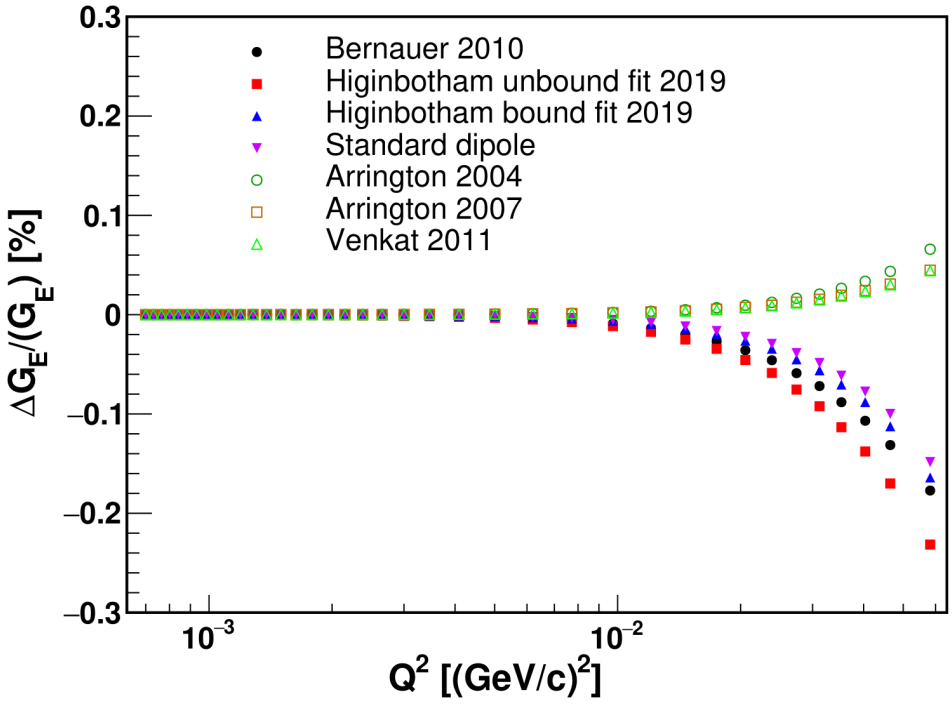


Figure S12: Relative difference between the extracted $G_E^p$ when using the Kelly parametrization [12] for $G_M^p$ compared to a range of other parametrizations as listed in the legend [2,13–16].

## Charge Radius Extraction

We obtain $r_p$ from the extracted $G_E^p(Q^2)$ by fitting to a functional form and extrapolating to $Q^2 = 0$. Lower order functional forms such as the monopole, dipole, and the first order expansion of $Q^2$ tend to give smaller uncertainties but have large biases depending on the input $G_E^p(Q^2)$ parametrization used, while higher order functional forms such as the third order $Q^2$ expansion and third order $z$ transformation tend to give large uncertainties (see Figure S15). We have shown [17] that consistent results with the least uncertainties can be achieved when using the multi-parameter rational-function (referred to as Rational (1,1), described in the main text) or the second order polynomial expansion of $z$ [18], which takes the form of:

$$f(Q^2) = nG_E(Q^2) = n(1 + p_1 z + p_2 z^2), \tag{2}$$

after making a conformal mapping through [18]:

$$z = \frac{\sqrt{T_c + Q^2} - \sqrt{T_c - T_0}}{\sqrt{T_c + Q^2} + \sqrt{T_c - T_0}}, \tag{3}$$

where $T_c = 4m_\pi^2$, $m_\pi$ is the mass of a $\pi^0$ meson, and $T_0$ is a free parameter representing the point that is mapping onto $z = 0$ ($T_0 = 0$ for this study). The charge radius is given by $r_p = \sqrt{-3p_1/2T_c}$.

Both functional forms describe the data well, with a reduced $\chi^2$ of $\sim 1.3$ when considering only the statistical uncertainty. The fit of $G_E^p(Q^2)$ with the Rational (1,1) function is shown with its $1\sigma$ band in Figure S13. Also shown are the results from a previous high precision spectrometer based $e - p$ experiment [19] and the calculation by Alarcon *et al.* [20]. The quality of the fit is shown in Figure S14 where **a** shows the residuals of the fit, and **b** shows the pull distribution. The largest

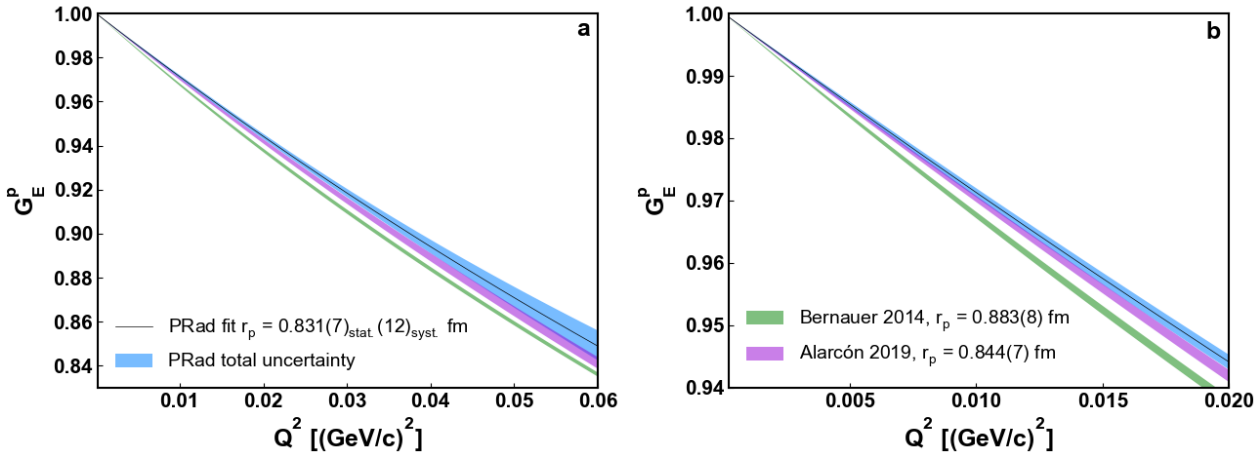


Figure S13: The $1\sigma$ band of the Rational (1,1) fit to the $G_E^p(Q^2)$ extracted from the PRad data (blue). Also shown are the fits from a previous high-precision, magnetic spectrometer based $e-p$ experiment [19] (green) and the calculation of Alarcon *et al.* [20] (purple). **(a)** The entire PRad data set, **(b)** a view of the $Q^2 < 0.02$ (GeV/c)$^2$ range.

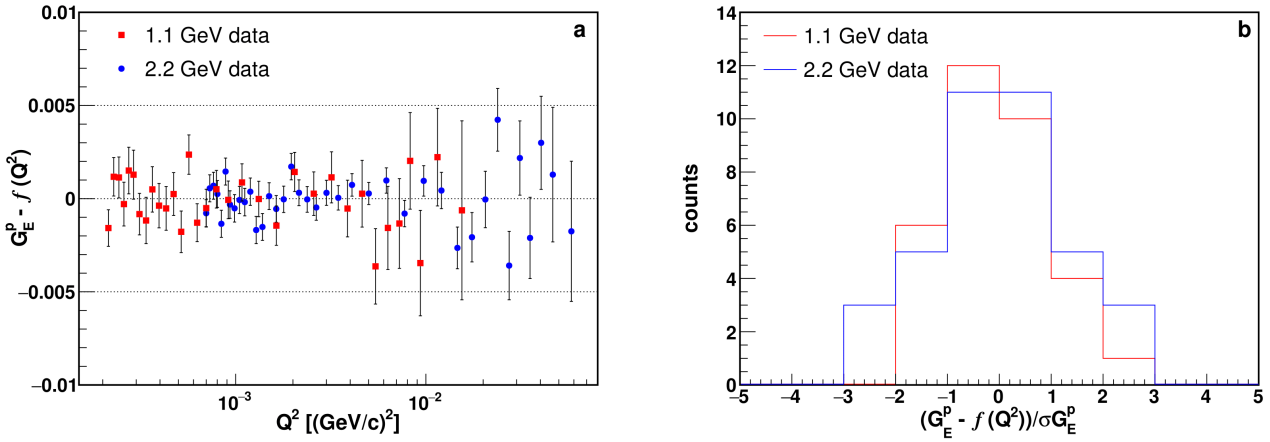


Figure S14: **(a)** The residuals of the fit of $G_E^p(Q^2)$ using the Rational (1,1) function. Error bars show the statistical uncertainty. **(b)** pull distribution of the same fit.

deviation is about 2.5 standard deviations. We also extracted $r_p$ using a number of other commonly used functional forms, as shown in Figure S15. These results confirm our earlier finding [17] that

lower order functional forms such as the monopole, dipole, and the first order expansion of $Q^2$ (not shown here) tend to give smaller statistical uncertainties, but have larger uncertainties from the truncation of the $Q^2$ range and the extrapolation to $Q^2 = 0$ and also larger biases depending on the input $G_E^p(Q^2)$ parametrization used. On the other hand higher order functional forms such as the third order $Q^2$ expansion (not shown here) and $z$ transformation [18] tend to give very large overall uncertainties. The results also confirm that Rational (1,1) and second order $z$ transformation are the most robust fit functions, giving the most consistent results with the least uncertainties for the $Q^2$ range of the PRad experiment. The consistency of the radius extraction was further studied

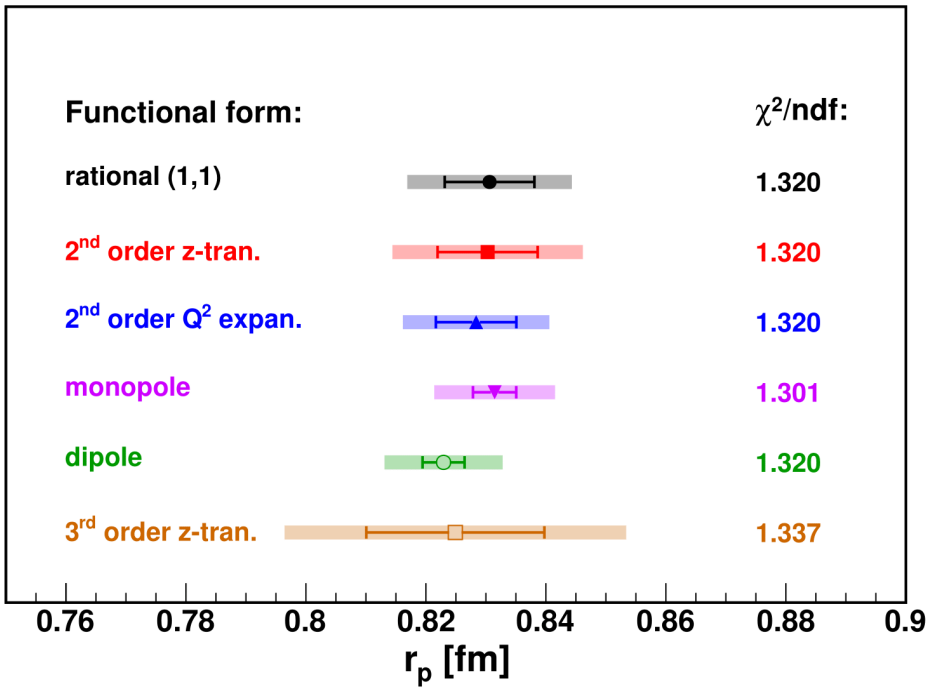


Figure S15: The $r_p$ results obtained when using different functional forms. Statistical uncertainties are shown as error bars, and the total uncertainties are shown as colored bands. Rational(1,1) and second order $z$ transformation are identified as robust fit functions by Yan *et al.* [17].

by extracting $r_p$ from various sub-sets of the experimental data, such as the data collected with only the 1.1 GeV electron beam, only the 2.2 GeV electron beam, just the $PbWO_4$ modules, and the $Q^2$ range limited to $< 0.016$ (GeV/c)$^2$ and $> 0.002$ (GeV/c)$^2$. All the data sub-sets were fitted with the Rational (1,1) functional form and the $r_p$ values obtained are consistent within statistical uncertainty as shown in Figure S16 (a). However, the $r_p$ values extracted from some data sub-sets, such as the ones with restricted $Q^2$ range, have larger uncertainty because the $Q^2$ coverage is reduced, and the Rational (1,1) is not the most robust functional form for these data sub-sets. This is demonstrated in Figure S16 (b), where the 1.1 GeV and 2.2 GeV data sets are separately fitted using the two best functional forms for these particular data sets, as determined from the robustness study [17].

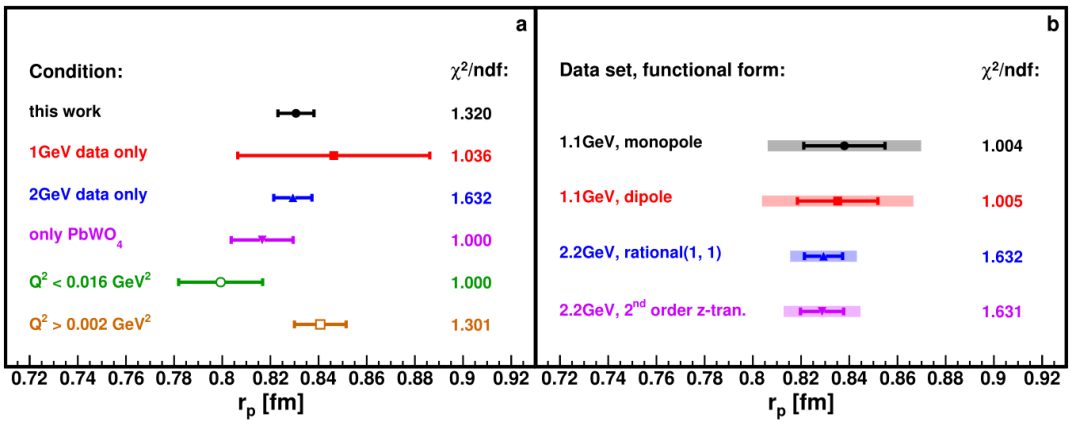


Figure S16: **(a)** The $r_p$ results obtained when using different data sub-sets fit with the Rational (1,1) function. Only the statistical uncertainties are shown here. **(b)** The $r_p$ results obtained when using different data sub-sets but fit with the two best functional forms for these chosen data sub-sets, as determined from the robustness study [17].

## Systematic Uncertainties

The Systematic uncertainties of the PRad experiment are grouped into uncorrelated uncertainties and correlated ones. The latter are further divided into normalization type uncertainty and $Q^2$ dependent uncertainty. Table S1 shows a complete list of known systematic uncertainties and their effects on $r_p$ and the normalization parameters. Event selection consists of a series of cuts to distinguish between $e-p$ elastic and $e-e$ events, and it is dominated by the elastic cut. Changes in the elastic cut can cause small variations in the extracted cross section, but they are not uniform across the different detector modules of HyCal. The changes are non-uniform because of small inter-module differences in properties such as light attenuation, non-linearity of detector response and microscopic gaps between detector modules. These cause a small non-uniformity in the agreement between the simulated energy spectrum and the data spectrum. The effect of this systematic uncertainty was studied by varying the elastic cut over a wide range (at 2.2 GeV for example, $1.75\sigma$ to $5.25\sigma$ - the $PbWO_4$ resolution) to cover all the possible module-to-module discrepancies. The variation of the elastic cut leads to changes in the extracted cross section of $0.1\%$, on average, and is typically bounded by $\pm$ $0.15\%$. The variation in $r_p$ from this change in the extracted cross section was assigned as the uncertainty due to event selection. The influence of detector efficiency, beam background, HyCal response, acceptance and beam energy on the extraction of the cross section and form factor was studied by varying each of these factors, one at a time, in either the simulation or data and comparing the smeared and un-smeared results. The inelastic $e-p$ contribution, $G_M^p$ parameterization and the radiative correction depend on input models, hence their uncertainties are determined by changing the parameters of the model or by

| Item | $r_p$ uncertainty (fm) | $n_1$ uncertainty | $n_2$ uncertainty |
|---|---|---|---|
| Event selection | 0.0070 | 0.0002 | 0.0006 |
| Radiative correction | 0.0069 | 0.0010 | 0.0011 |
| Detector efficiency | 0.0042 | 0.0000 | 0.0001 |
| Beam background | 0.0039 | 0.0017 | 0.0003 |
| HyCal response | 0.0029 | 0.0000 | 0.0000 |
| Acceptance | 0.0026 | 0.0001 | 0.0001 |
| Beam energy | 0.0022 | 0.0001 | 0.0002 |
| Inelastic $ep$ | 0.0009 | 0.0000 | 0.0000 |
| $G_M^p$ parameterization | 0.0006 | 0.0000 | 0.0000 |
| Total | 0.0115 | 0.0020 | 0.0013 |

Table S1: Systematic uncertainty table for $r_p$ and the normalization parameters. Items are arranged in decreasing order of the effect on $r_p$. The parameters $n_1$ and $n_2$ are the normalization parameters for 1.1 GeV and 2.2 GeV respectively. Uncertainties are estimated using the Rational (1,1) function.

using a variety of models. The inelastic contribution to the cross section is simulated using the Christy 2018 empirical fit [10] to existing data. It produces a good agreement between the data and simulation, with at most a 10% difference for the amplitude and a 0.5% difference for the position of the $\Delta$-resonance peak, for the $PbWO_4$ detector region. Similar conclusion can be drawn if one uses the MAID 2007 model [21]. The inelastic model is then scaled and shifted by the difference between data and simulation, to determine its systematic uncertainty on $r_p$ extraction. The systematic uncertainty due to the choice of $G_M^p$ parameterization is determined by assuming a wide range of $G_M^p$ parameterizations [2,13–16], including the standard dipole model, and comparing the result with those obtained from the Kelly [12] parametrization. As shown in Figure S12, the difference is $< 0.01\%$ in the $Q^2 < \ 0.01\ (\mathrm{GeV/c})^2$ region, and the largest difference is at the level of 0.2%, for the Higinbotham 2019 unbound fit [16] which is based on the Mainz data set [1]. The same parameterization also gives the largest variation in $r_p$, which is about 0.001 fm. The uncertainty due to the radiative corrections arises mainly from neglecting the higher order contributions to the cross sections for both $e-p$ elastic and $e-e$ processes. It is estimated based on the approach by Arbuzov and Kopylova [22]. The cross section is varied within the estimated range and the change in the extracted $r_p$ is recorded as the uncertainty. A Monte Carlo technique was used to randomly smear the cross section and $G_E^p$ data points for each of the systematic uncertainty mentioned above. The $r_p$ was extracted from the smeared data and the process is repeated 100,000 times. The RMS of the resulting distribution of $r_p$ is recorded as the systematic uncertainty. The total systematic uncertainty is 1.4%.

1. Bernauer, J. C. *et al*. High-precision determination of the electric and magnetic form factors of the proton. *Phys. Rev. Lett.* **105**, 242001 (2010).

2. Bernauer, J. C. *Measurement of the Elastic Electron-proton Cross Section and Separation of the Electric and Magnetic Form Factor in the $Q^2$ Range from 0.004 to 1 (GeV/c)$^2$* (Ph.D. Thesis, Inst. Kernphys, Johannes Gutenbeg-Universitat, Mainz, Germany., 2010).

3. Gasparian, A. A high performance hybrid electromagnetic calorimeter at jefferson Lab. In Cecchi, C., Cenci, P., Lubrano, P. & Pepe, M. (eds.) *Proc. XI Int. Conf. Calorim. Part. Phys.*, 109–115 (World Scientific, Singapore, 2005).

4. Sober, D. I. *et al*. The bremsstrahlung tagged photon beam in Hall B at JLab. *Nucl. Instr. Meth. A* **440**, 263–284 (2000).

5. Akushevich, I., Gao, H., Ilyichev, A. & Meziane, M. Radiative corrections beyond the ultra relativistic limit in unpolarized ep elastic and Møller scatterings for the PRad Experiment at Jefferson Laboratory,. *Eur. Phys. J. A* **51**, 2015–15001 (2015).

6. Tomalak, O. Two-photon exchange correction in elastic lepton-proton scattering. *Few Body Syst.* **59**, 87 (2018).

7. Tomalak, O. & Vanderhaeghen, M. Two-photon exchange correction in elastic unpolarized electron-proton scattering at small momentum transfer. *Phys. Rev. D* **93**, 013023 (2016).

8. Tomalak, O. & Vanderhaeghen, M. Subtracted dispersion relation formalism for the two-photon exchange correction to elastic electron-proton scattering: Comparison with data. *Eur. Phys. J. A* **51**, 24 (2015).

9. Gramolin, A. V. *et al*. A new event generator for the elastic scattering of charged leptons on proton. *J. Phys. G* **41**, 115001 (2014).

10. Christy, M. E. & Bosted, P. E. Empirical fit to precision inclusive electron-proton cross-sections in the resonance region. *Phys. Rev. C* **81**, 055213 (2010).

11. Gasparian, A., Khandaker, M., Gao, H. & Dutta, D. A proposal for Jefferson Laboratory: High Precision Measurement of the Proton Charge Radius. `https://www.jlab.org/exp_prog/proposals/12/c12-11-106.pdf` (2011). JLab PAC39 proposal C12-11-106.

12. Kelly, J. J. Simple parametrization of nucleon form factors. *Phys. Rev. C* **70**, 068202 (2004).

13. Venkat, S., Arrington, J., Miller, G. A. & Zhan, X. Realistic transverse images of the proton charge and magnetic densities. *Phys. Rev. C* **83**, 015203 (2011).

14. Arrington, J. Implications of the discrepancy between proton form-factor measurements. *Phys. Rev. C* **69**, 022201 (2004).

15. Arrington, J. & Sick, I. Precise determination of low-Q nucleon electromagnetic form factors and their impact on parity-violating e-p elastic scattering. *Phys. Rev. C* **76**, 035201 (2007).

16. Higinbotham, D. W. & McClellan, R. E. How analytic choices can affect the extraction of electromagnetic form factors from elastic electron scattering cross section data. *arXiv:1902.08185* (2018).

17. Yan, X. *et al*. Robust extraction of the proton charge radius from electron-proton scattering data. *Phys. Rev. C* **98**, 025204 (2018).

18. Lee, G., Arrington, J. R. & Hill, R. J. Extraction of the proton radius from electron-proton scattering data. *Phys. Rev. D* **92**, 013013 (2015).

19. Bernauer, J. C. *et al*. Electric and magnetic form factors of the proton. *Phys. Rev. C* **90**, 015206 (2014).

20. Alarcon, J. M., Higinbotham, D. W., Weiss, C. & Ye, Z. Proton charge radius from electron scattering data using dispersively improved chiral effective field theory. *Phys. Rev. C* **99**, 044303 (2019).

21. Drechsel, D., Kamalov, S. S. & Tiator, L. Unitary isobar model - maid2007. *Eur. Phys. J. A* **34**, 69 (2007).

22. Arbuzov, A. A. & Kopylova, T. V. On higher order radiative corrections to elastic electron-proton scattering. *Eur. Phys. J. C.* **75**, 603 (2015).